PCCP

PAPER

View Article Online
View Journal | View Issue

Check for updates

Cite this: *Phys. Chem. Chem. Phys.*, 2025, **27**, 18302

Tunable synthesis of carbon nanotubes *via* methane catalytic pyrolysis by adjusting Mo incorporation in Fe/MgO

Zeyou Pan, [ab] Frank Krumeich, [b] Paweł P. Ziemiański[cd] and Jeroen A. van Bokhoven *[ab]

Received 6th November 2024,
Accepted 7th August 2025

DOI: 10.1039/d4cp04231j

rsc.li/pccp

Catalytic pyrolysis of methane for the synthesis of carbon nanotubes (CNTs) was explored using an Fe–Mo/MgO catalyst. The impact of molybdenum (Mo) addition on carbon productivity and product characteristics was investigated by (S)TEM, XRD, TGA, nitrogen adsorption, and Raman spectroscopy. The Fe/MgO catalyst exhibited a carbon productivity of 0.16 g $g_{Cat.}^{-1}$ with 15% graphitic carbon selectivity. TEM revealed that carbon nanotubes (CNTs) including single-walled (SWCNTs) and double-walled nanotubes (DWCNTs) were produced. Mo incorporation synergistically enhanced both carbon productivity and graphitic carbon selectivity. For Fe-0.1Mo, productivity improved to 0.40 g $g_{Cat.}^{-1}$ with 60% graphitic carbon selectivity, while preferentially yielding SWCNTs. Further increasing Mo loading maximized productivity at 1.03 g $g_{Cat.}^{-1}$ for Fe–1Mo, coupled with 96% graphitic carbon selectivity. At higher Mo concentrations (Fe–0.5Mo and Fe–1Mo), Fe–Mo nanoparticle coarsening occurred, shifting CNT morphology toward multi-walled structures (MWCNTs). Lifetime studies confirmed enhanced catalyst stability under Mo promotion, with Fe–1Mo remaining active beyond 1 hour. Conversely, Mo/MgO showed negligible activity (0.08 g $g_{Cat.}^{-1}$) and produced only graphite flakes, underscoring iron's essential role in CNT growth. This work demonstrates Mo's dual function in enabling selective CNT production while providing mechanistic insights into its promotion of methane pyrolysis and nanotube formation.

Open Access Article. Published on 12 August 2025. Downloaded on 5/25/2026 12:26:41 AM.
This article is licensed under a Creative Commons Attribution-NonCommercial 3.0 Unported Licence.

1. Introduction

Methane pyrolysis for the production of clean hydrogen (H_2) has gained significant interest.[1–5] Methane steam reforming (MSR), a conventional hydrogen production technology, inherently generates substantial CO_2 emissions. In contrast, methane pyrolysis offers a CO_2-free alternative by directly decomposing methane into hydrogen and solid carbon. The standard reaction enthalpy for methane pyrolysis (37.7 kJ mol^{-1} H_2) is significantly lower than that of steam reforming (63.4 kJ mol^{-1} H_2), suggesting superior thermodynamic efficiency for pyrolysis under comparable conditions.[3,6] While water electrolysis represents another promising CO_2-free hydrogen production method, its considerably higher reaction enthalpy (285.8 kJ mol^{-1} H_2) entails substantially greater energy input relative to both methane-derived processes. Although methane pyrolysis has obvious advantages, the economic viability of methane pyrolysis is hampered by the low market value of carbon black and the high costs associated with the technology.[3]

To tackle these challenges, a catalyst was employed to augment the reaction efficiency and the quality of carbon.[3,4,7] Metal oxides (Al_2O_3, MgO, and SiO_2) that incorporate transition metals (Fe, Co, and Ni) are frequently utilized as catalysts.[3,8–10] These catalysts lower the reaction temperature, enhance H_2 selectivity, and transform carbon into high-value CNTs.[11–13] Depending on the size of the metal particles, various types of CNTs (single walled – SW; double-walled – DW; multi-walled – MW) with different diameters can be produced.[9,14,15] Lamouroux *et al.* observed that SW- and DWCNTs are typically produced on catalysts with metal particles smaller than 5 nm, while MWCNTs are predominantly formed on catalysts with larger metal particles.[9] To regulate the formation of CNTs, a straightforward approach includes the adjustment of the metal loading. Excessive metal loading can saturate the surface of the substrate, leading to metal aggregation, whereas low loading (<5 wt%) results in a high dispersion of metal with a small particle size. Furthermore, a second metal is commonly employed to increase enhancement.[3,9] Wang *et al.* explored the effect of adding various metals (Cu, Co, Fe, Mn, Pd, Zn, and Mg) on Ni/Al_2O_3 and observed that the presence of a second metal enhances methane conversion; the addition of Mg

[a] *Center for Energy and Environmental Sciences, Paul Scherrer Institute, 5232 Villigen, Switzerland*
[b] *Institute for Chemical and Bioengineering, Department of Chemistry and Applied Biosciences, ETH Zurich, 8093 Zurich, Switzerland. E-mail: jeroen.vanbokhoven@chem.ethz.ch*
[c] *Building Energy Materials and Components, Empa, 8600 Dübendorf, Switzerland*
[d] *Laboratory for Computational Engineering, Empa, 8600 Dübendorf, Switzerland*

 This journal is © the Owner Societies 2025

Open Access Article. Published on 12 August 2025. Downloaded on 5/25/2026 12:26:41 AM.
This article is licensed under a Creative Commons Attribution-NonCommercial 3.0 Unported Licence.

specifically optimizes the morphology of the carbon nanofibers (CNFs).[16] Torres *et al.* incorporated molybdenum (Mo) into iron catalysts and demonstrated that it enhances both methane conversion and the structural arrangement of CNTs.[17] Yeoh *et al.* reported that the addition of a small amount of Mo favors metal dispersion and prevents the aggregation of active metal particles.[18] Numerous studies have demonstrated that Mo can enhance methane decomposition and facilitate the production of CNTs.[17–21] Despite extensive research on bimetallic catalysts, the mechanistic role of secondary metals remains incompletely understood.

In this study, the influence of Mo loading on catalyst properties, reaction kinetics, and carbon product formation were investigated using Fe/MgO catalyst. Various analytical techniques, such as X-ray diffraction (XRD), thermogravimetric analysis (TGA), scanning/transmission electron microscopy ((S)TEM), nitrogen gas adsorption, and Raman spectroscopy, were comprehensively employed for elucidating the promotion mechanism of Mo and advance the fundamental understanding of its role in governing CNT growth, providing mechanistic insights for controlling CNT production.

2. Experimental section

2.1. Materials

Magnesium oxide (MgO, ≥97%), iron(III) nitrate nonahydrate ($Fe(NO_3)_3{\cdot}9H_2O$, ≥98%), ammonium molybdate tetrahydrate ($(NH_4)_6Mo_7O_{24}{\cdot}4H_2O$, ≥99.0%), carbon black, and multi-walled carbon nanotubes (MWCNTs, 95%, 20–50 nm in diameter, 1–5 μm in length) were purchased from Fluka, Sigma-Aldrich, Honeywell-Fluka, Cabot, and Nanolab.

2.2. Catalyst preparation

The catalysts are synthesized by impregnation and hydrothermal treatment.[22,23] Commercial MgO powder and metal precursor were dissolved in deionized water respectively and mixed. The suspension was then sonicated for 10 min. Afterwards, hydrothermal treatment was performed at 200 °C in an autoclave for 2 h. After cooling down to room temperature, the suspension was dried at 100–120 °C, and the residual solid was crushed into powder that was finally used as fresh catalyst.

Regarding the fraction of Fe/MgO and Fe–Mo/MgO, Fe content were 0.03 mol mol^{-1} MgO. Mo as the second metal in Fe–Mo/MgO, the contents were 0.1, 0.5 and 1 mol mol^{-1} Fe, respectively. In Mo/MgO, Mo content was 0.03 mol mol^{-1} MgO. All catalysts are denoted as Fe/MgO, Fe–0.1Mo, Fe–0.5Mo, Fe–1Mo, and Mo/MgO, respectively.

2.3. Catalytic pyrolysis of CH_4 for carbon nanotube (CNT) synthesis

The experiments were performed in a horizontal quartz tube. 150 mg fresh catalyst was put on a porcelain boat and heated up to 850 °C with 10 °C min^{-1} rate in Helium. Then, temperature was kept at 850 °C for 30 min meanwhile pure CH_4 with 20 mL min^{-1} flow rate was introduced. After reaction, the reactor was cooled down in Helium atmosphere. Samples were eventually preserved for further characterization.

2.4. Catalysts characterization

(Scanning) transmission electron microscopy ((S)TEM). For (S)TEM investigation, the material was dispersed in ethanol and a few drops of the suspension were deposited onto a perforated carbon foil supported on a copper grid. After evaporation of the ethanol, the grid was mounted on the single tilt holder of the microscope. (S)TEM investigations were performed on JEM-F200 (JEOL) microscope, operated at an acceleration potential of 200 kV (cold field emitter). In STEM, detectors can be selected for imaging in bright field (BF) and annular dark field (ADF) mode. TEM images were recorded with a 16 M pixel CMOS camera (Rio, Gatan). Analytical investigations were done with two energy-dispersive X-ray spectrometers (EDXS, JEOL) attached to the microscope column.

Raman spectroscopy. Raman spectroscopy (Horiba Raman, LabRAM HR Evolution UV-VIS-NIR, Nd: YAG, exciting at λ = 532 nm) were used to evaluate the graphitization degree of the deposited carbonaceous products. Regarding the spectra acquisition, 2–4 different points over the sample surface are chosen for spectra recording and the spectra of every point are recorded three times.

Thermogravimetric analysis (TGA). TGA was conducted on a TGAQ50 (TA Instruments) instrument to evaluate the quantity and the thermal stability of accumulated carbonaceous products. In detail, the samples were heated up from 50 to 1000 °C with 20 °C min^{-1} heating rate in an ambient air atmosphere with a flow rate of 50 mL min^{-1}.

$$\text{Carbon productivity} = \frac{[\text{Weight loss}]}{[\text{Residual weight}]}\left(\text{g g}_{\text{Cat.}}{}^{-1}\right)$$

X-ray diffraction (XRD). XRD were measured on a Bruker D8 diffractometer using Cu Kα radiation with a wavelength of 1.5456 Å. The data were recorded with 0.02° per step within the range of 10–90° 2θ.

H_2-temperature programmed reduction (H_2-TPR). Before doing H_2-TPR, all fresh catalysts were calcined at 850 °C with N^2 atmosphere. H_2-TPR were carried out using a Micrometrics Autochem 2950 HP unit equipped with a TCD. Samples (*ca.* 40–80 mg) were loaded in a U-shaped quartz cell. In a standard experiment, a continuous flow of 20 mL min^{-1} of 10% vol H_2 in Ar was fed to the cell while increasing the temperature (10 °C min^{-1}) to 800 °C; the output passed through a cold trap (isopropanol + liquid nitrogen) before reaching the TCD detector.

Microtexture characterization by N_2 adsorption. Nitrogen adsorption measurements were carried out using a Micromeritics 3Flex device. For each measurement, 6 to 40 mg of sample material was weighed into glass sample tubes and subjected to activation under high vacuum (~0.001 mbar) at 180 °C for 24 hours using the degassing station. Adsorption and desorption isotherms were obtained at the temperature of liquid nitrogen (77.3 K), with relative pressures reaching up

Open Access Article. Published on 12 August 2025. Downloaded on 5/25/2026 12:26:41 AM.
This article is licensed under a Creative Commons Attribution-NonCommercial 3.0 Unported Licence.

to 0.998 p/p_0. To determine the pore size distribution, the nonlocal density functional theory (NLDFT) model implemented in the Flex 6.02 software (Micromeritics) was applied using a kernel tailored for cylindrical pores in multi-walled carbon nanotubes (N2@77–Carb Cyl Pores, MWNT) and single-walled carbon nanotubes (N2@77-Carb Cyl Pores, SWNT).

3. Results and discussion

3.1. Characterization of fresh catalysts

Before conducting the experiments, all fresh catalysts were comprehensively evaluated by (S)TEM, XRD, TGA, and H_2-TPR. Details regarding the synthesis of the catalysts are given in the Experimental section. Fig. 1 depicts the morphology (a–e) and chemical composition (f) of the catalysts; the Fe–Mo/MgO catalysts are denoted as Fe–0.1Mo, Fe–0.5Mo, and Fe–1Mo. The images in Fig. 1a–e reveal that all the catalysts exhibited a predominantly sheet-like structure with a thickness ranging from 4 to 20 nm and lateral dimensions in the hundreds of nanometres. According to Yu *et al.*, the nano-sheet structure was attributed to $Mg(OH)_2$, formed by the hydration of magnesium oxide by means of the oriented attachment of nanocrystals,[24] which is verified by XRD analysis in Fig. 1f (*vide infra*). To investigate the dispersion of metal elements on $Mg(OH)_2$, energy-dispersive X-ray spectroscopy (EDS) was employed. As shown in the insets in Fig. 1a–e, Fe and Mo elements exhibited uniform dispersion on $Mg(OH)_2$, without any discernible particles across all catalysts. This can be attributed to the nanosheet structure, which provided ample surface area for the dispersion of metal species. Furthermore, $Mg(OH)_2$ hydrates exhibited a strong interaction with metal species, thereby facilitating the dispersion of metals.[23]

XRD was utilized to examine the chemical composition of the catalysts (Fig. 1f). The diffraction peaks detected at 2θ values of 18.7, 33.0, 38.1, 51.0, 58.9, 62.3, 72.4, and 81.5° were indicative of the $Mg(OH)_2$ phase, observed in all the catalysts. In the XRD pattern of the Fe-based catalysts, the presence of $FeMg_3O_{10}$ was confirmed by the 2θ values of 11.2, 22.6, and 34.1°. The peak at 11.2° exhibited a slight increase with the Mo addition, suggesting that Mo promotes the formation of $FeMg_3O_{10}$. Since Fe predominantly occupied the $Mg(OH)_2$ surface, excess Mo species presented as $H_2MoO_4{\cdot}H_2O$ (Fig. 1f, at 12.8°) which was gradually enhanced with Mo addition. With the absence of Fe, however, Mo species, like MoO_x, may interacted with $Mg(OH)_2$ in Mo/MgO, leading to the formation of $H_{10}MgMoO_9$. It was verified by the observation of $H_{10}MgMoO_9$ in 0.06Mo/MgO and 0.12Mo/MgO catalyst (Fig. S1). With the increase of Mo loading, excess Mo presented as MoO_x and $H_2MoO_4{\cdot}H_2O$ in 0.12Mo/MgO, demonstrating the hypothesis of $H_2MoO_4{\cdot}H_2O$ in Fe–xMo catalyst.

Besides, the reducibility of Fe/MgO, Fe–xMo and Mo/MgO was compared by H_2-TPR (Fig. S2). Fe/MgO initiates reduction at approximately 250 °C, which is possibly contributed by the reduction of Fe_2O_3 to Fe_3O_4.[17] In addition, the broad peak between 450 to 800 °C is associated with Fe_3O_4 reduction. In Fe–0.1Mo, the Mo addition slightly shifts the reduction temperature to *ca.* 350 °C but the reduction pattern was similar to that of Fe/MgO. By enhancing the Mo loading, the initial reduction temperature is up to *ca.* 450 °C in Fe–0.5Mo and the reduction pattern is closing to that of Mo/MgO with a reduction temperature above 500 °C, contributing by the

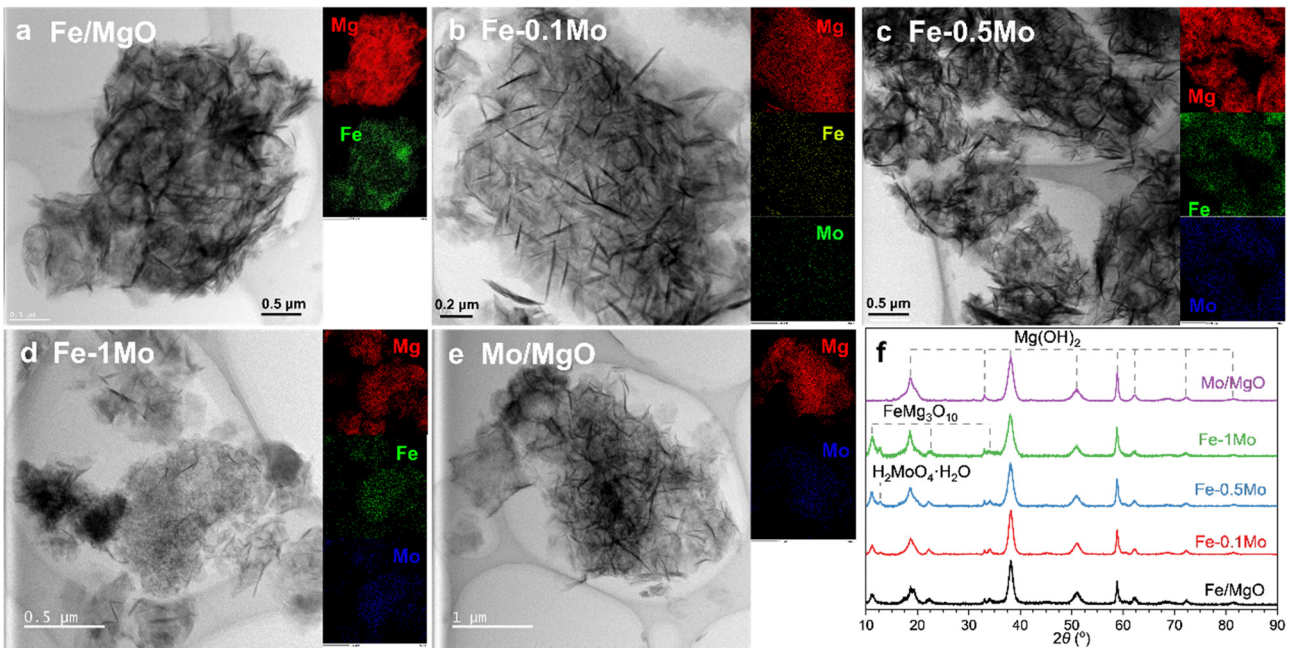

Fig. 1 The morphology and phase composition of fresh catalysts. (a)–(e) STEM images of all fresh catalysts (Fe/MgO, Fe–Mo/MgO and Mo/MgO) in bright field mode. Insets: Energy-dispersive X-ray spectra (EDS) mapping of Mg, Fe and Mo elements on different catalysts. (f) Phase composition and crystalline structure of all fresh catalysts as revealed by XRD.

 This journal is © the Owner Societies 2025

Open Access Article. Published on 12 August 2025. Downloaded on 5/25/2026 12:26:41 AM.
This article is licensed under a Creative Commons Attribution-NonCommercial 3.0 Unported Licence.

reduction of MoO_3 to MoO_2 (500–620 °C) and MoO_2 to metallic Mo (>620 °C).[8,25] These results suggest that Mo incorporation inhibits the reducibility of the Fe–*x*Mo catalysts.[17]

3.2. Evaluation of carbon products

In the catalytic pyrolysis of methane, fresh catalysts were subjected to heating up to 850 °C and were then maintained at this temperature for 30 minutes. After cooling, the carbon deposits were analysed. Fig. 2a–e and Fig. S3 show the TEM images of spent catalysts. CNT growth was observed on Fe/MgO catalysts (Fig. 2a and Fig. S3). Both SW- and DW-CNTs were clearly identified in Fig. 2a. Further TEM imaging (Fig. S3) revealed numerous long carbon nanotubes adhering tortuously to the catalyst surface (randomly and entangled). After separation using an HCl dissolution to remove the catalyst, the inner diameters of the separated CNTs grown on Fe/MgO catalysts were analysed (Fig. 2a inset) based on nitrogen measurements (Fig. S4) using SWNT NLDFT model. The inner diameters were predominantly distributed between 3–10 nm, with an average inner diameter of 6.2 nm. On the Fe–0.1Mo catalyst, a large number of SWCNTs, attaching to the catalyst surface in either an erect or lying-down orientation, were observed (Fig. 2b and Fig. S3). The inner diameters of the CNTs mainly ranged from 3–15 nm (Fig. 2b inset), with an average diameter of 7.9 nm. With increasing Mo loading, MWCNTs dominated on the products of Fe–0.5Mo and Fe–1Mo catalysts (Fig. 2c, d and Fig. S3), whose average inner diameters were enlarged to 13.6 nm and 15.7 nm, respectively. This demonstrates that Mo addition progressively enlarges CNT diameters. Based on the principle that metal particle size determines CNT diameter,[9] it results out that the Mo incorporation increases the average diameter of Fe particles.

In contrast, Mo/MgO exhibited graphitic layers with an interlayer spacing of 0.48 nm (Fig. 2e and Fig. S3), consisting with graphene structure, while no evidence of CNT formation was observed. It suggests that Mo alone does not actively facilitate CNT growth, further supporting the conclusion that Fe is indispensable for initiating and sustaining nanotube formation under these conditions.

The quantification of the deposited carbon was determined by TGA (Fig. S5) and the carbon productivity is illustrated in Fig. 2f (red column). Fe/MgO exhibits a carbon productivity of 0.16 g $g_{Cat.}^{-1}$. Upon introducing Mo, the carbon productivity was gradually enhanced. In Fe–0.1Mo, specifically, the carbon productivity reached 0.40 g $g_{Cat.}^{-1}$, which is further improved and reached the maximum, 1.03 g $g_{Cat.}^{-1}$, on Fe–1Mo. This

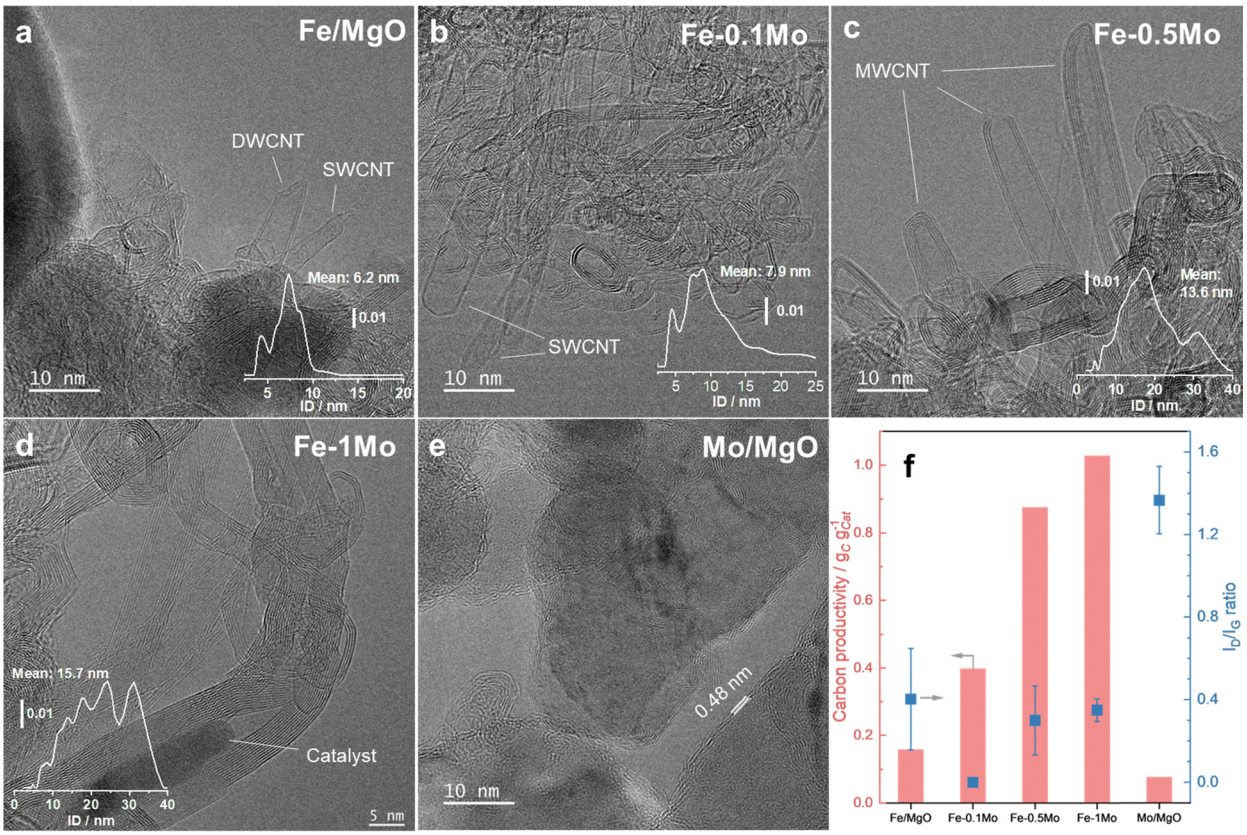

Fig. 2 TEM images of different spent catalysts with respective insets of CNT inner diameter distribution calculated with NLDFT method. The average pore diameter was calculated using pores with < 40 nm inner diameter. (a)–(e) Are Fe/MgO, Fe–0.1Mo/MgO, Fe–0.5Mo/MgO, Fe–1Mo/MgO, and Mo/MgO, respectively. (f) The carbon productivity (in 30 min, red column) and graphitization (blue square) of different catalysts. The carbon graphitization is described by the ratio of the D (1210–1430 cm^{-1}) to the G band (1430–1685 cm^{-1}) of the Raman spectra (Fig. S4), in which the D band is ascribed to the structural disorder in graphitic layers and G band is attributed to the sp^2 hybridized in-plane carbon–carbon stretching vibrations.

Open Access Article. Published on 12 August 2025. Downloaded on 5/25/2026 12:26:41 AM.
This article is licensed under a Creative Commons Attribution-NonCommercial 3.0 Unported Licence.

result underscores the synergistic role of Mo in enhancing the catalytic activity of Fe toward carbon production. In contrast, the Mo/MgO catalyst alone displays negligible carbon productivity (0.08 g $g_{Cat.}^{-1}$), indicating that Mo does not independently drive carbon formation. These findings collectively highlight Fe as the primary active component responsible for carbon production, with Mo serving as a promoter that optimizes Fe's catalytic performance.

Carbon products were classified by thermal stability (Fig. S5b), with a critical threshold of 600 °C distinguishing amorphous carbon (<600 °C) from graphitic carbon (>600 °C). In the Fe/MgO system, graphitic carbon constituted only 15% of the total carbon species. However, the incorporation of Mo significantly enhanced graphitization. For Fe–Mo/MgO catalysts, the proportion of graphitic carbon rose to 59.9% (Fe–0.1Mo) and reached a maximum of 96.2% (Fe–1Mo), demonstrating a strong Mo-loading dependence. Notably, the Mo/MgO system exhibited intermediate graphitic carbon content (38.8%), likely attributable to the formation of a small amount of highly ordered graphene, as corroborated by TEM analysis. These findings underscore that while Mo synergistically amplifies Fe's graphitization capability, its standalone catalytic activity for graphitic carbon formation remains limited compared to Fe–Mo bimetallic systems.

Raman spectra (Fig. S6) was employed to assess the degree of carbon graphitization based on the ratio of the D band to the G band (I_D/I_G, Fig. 2f).[22] The D band, spanning 1210–1430 cm^{-1}, corresponds to structural disorder or defects within the graphite lattice, while the G band, observed between 1430–1685 cm^{-1}, arises from the in-plane stretching vibrations of sp^2 hybridized carbon–carbon bonds. This I_D/I_G ratio serves as a quantitative indicator of carbon graphitization, where a lower ratio typically reflects higher structural order and improved graphitization. Compared to Fe/MgO, an I_D/I_G ratio of 0.0 was observed on Fe–0.1Mo, indicating negligible structural defects and enhanced graphitic ordering within the CNT. This ratio is consistent with the observation of highly graphitized SWCNTs. When the Mo content was increased, the I_D/I_G ratios for Fe–0.5Mo and Fe–1Mo were 0.30 and 0.35, respectively. Based on TEM observations, it is inferred that MWCNTs are probably the primary carbon products on Fe–0.5Mo and Fe–1Mo. It is noteworthy that the CNTs synthesized on the Fe-based catalysts demonstrate lower I_D/I_G ratios than the commercial MWCNTs (with an I_D/I_G ratio of 0.87), indicating that these CNTs match the graphitic quality of commercially available counterparts. On Mo/MgO, the carbon product has an I_D/I_G ratio of 1.37, similar to that of commercial carbon black, which has an I_D/I_G ratio of 1.5 (Fig. 2f and Fig. S3).

3.3. Characterization of spent catalysts

The spent catalysts were characterized in order to understand the growth of CNT. Fig. 3a–e illustrates the morphology and metal-element dispersion of the spent catalysts. The nanosheet structure is absent on Fe-based catalysts, because $Mg(OH)_2$ is dehydrated to MgO upon heating,[23] as confirmed by XRD analysis (*vide infra*). This transformation results in the disruption of the nanosheet structure as well as the aggregation of particles of varying sizes on the substrate. EDS mapping provided information about the dispersion of Fe and Mo on the substrates. In Fe/MgO, Fe exhibits a good dispersion on the substrate, with the presence of only a few aggregated iron oxide particles of approximately 10 nm in diameter. The addition of Mo improves the dispersion of Fe, with Fe–0.1Mo and Fe–0.5Mo showing no observable iron or molybdenum particles. As the addition of Mo continues, the Mo particles (<50 nm) begin to sinter, with some Fe being present within these particles. This indicates that the metal dispersion on the

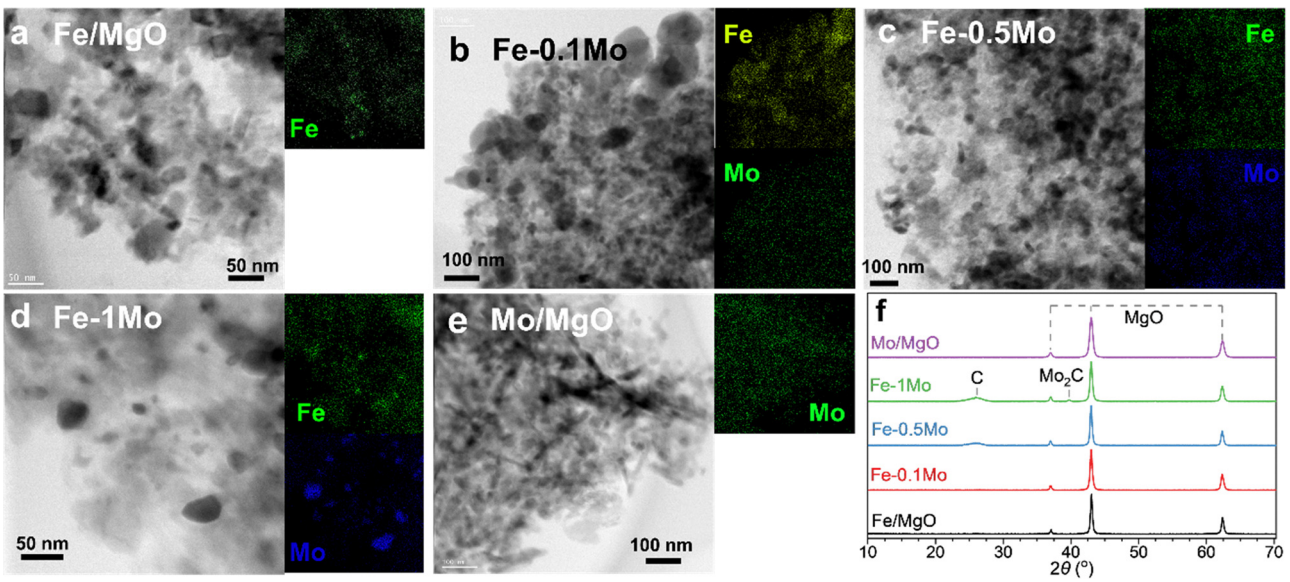

Fig. 3 The morphology and chemical compositions of spent catalysts. (a)–(e) STEM images of spent catalysts (Fe/MgO, Fe–Mo/MgO and Mo/MgO) recorded in bright field mode with EDS mapping images of Fe and Mo elements. (f) Phase composition and crystalline structure of spent catalysts using XRD.

 This journal is © the Owner Societies 2025

Open Access Article. Published on 12 August 2025. Downloaded on 5/25/2026 12:26:41 AM. This article is licensed under a Creative Commons Attribution-NonCommercial 3.0 Unported Licence.

substrate is limited by the metal loading, leading to sintering into particles at the higher loadings. In Mo/MgO, the morphology retains traces of a nanosheet-like structure (see the STEM image in Fig. 3e) and, importantly, Mo exhibits a uniform dispersion which may be due to the formation of $MgMoO_4$, a species with a high thermal stability.[8,26]

XRD revealed the chemical composition of the spent catalysts (Fig. 3f). The patterns of all the samples show diffraction peaks at 2θ values of 37.0, 43.0, and 62.4, attributed to the MgO phase, resulting from the $Mg(OH)_2$ dehydration at 250–550 °C (Fig. S7).[23,27] Carbon (002) phase was detected at *ca.* 25.0° in the patterns of Fe–0.5Mo and Fe–1Mo, and the intensity increased with Mo addition, aligning with the enhancement of carbon productivity (Fig. 2f). The presence of a Mo_2C signal at 39.7° in the Fe–1Mo pattern was caused by the carbon diffusion into Mo and nucleate into crystallites. Due to a low carbon productivity, the signal in the pattern of Fe–0.1Mo and Fe–0.5Mo were less pronounced. Compared with fresh catalyst, $FeMg_3O_{10}$ and $H_2MoO_4{\cdot}H_2O$ absented on spent catalysts which suggests that both were decomposed at high temperature.

3.4. Discussion of the mechanism

As a fresh catalyst, Fe precursor was homogeneously dispersed as $FeMg_3O_{10}$ on $Mg(OH)_2$ nanosheet and its crystallization notably enhanced by the introduction of Mo (Fig. 1f). In addition, an increase in Mo content correlated with a gradual intensification of H_2MoO_4 diffraction signals in XRD patterns, suggesting partial Mo segregation. However, EDX mapping (Fig. 1b–d) confirmed that the Fe dispersion was preserved even at elevated Mo loadings, indicating no adverse effects on spatial distribution.

As the reactor temperature increased, $Mg(OH)_2$ was dehydrated to MgO (Fig. S7). No distinct crystalline phases corresponding to Fe or Mo species were detected *via* XRD, likely due to the formation of non-crystalized species. H_2-TPR profiles revealed the sequential decomposition of Fe and Mo precursors into Fe_2O_3 and MoO_3 (Fig. S2), respectively. Intriguingly, the incorporation of Mo shifted the reduction temperature of Fe–Mo composites to higher temperature regimes. This phenomenon is attributed to the stabilization of Fe species within a $FeMoO_x$ interfacial structure, which likely impedes the reducibility of Fe_2O_3 by altering its electronic or coordinative environment.[25,28]

During the catalytic pyrolysis of methane, moderate agglomeration of Fe particles was observed (EDX mapping, Fig. 3a), which could be attributed to structural transformations induced by $Mg(OH)_2$ dehydration and thermal effects at elevated temperatures.[23] The incorporation of Mo in Fe–0.1Mo slightly enhanced Fe dispersion (Fig. 3b) by forming Fe–Mo bimetallic nanoparticles. Remarkably, Mo addition progressively increased carbon yield and significantly enhanced graphitic carbon selectivity. This synergistic effect may arise from the formation of molybdenum carbide phases (MoC_2), which can facilitate carbon atom diffusion across metal surfaces,[29] thereby optimizing CH_4 decomposition and carbon graphitization. Continuous incorporation of Mo promotes the coarsening of Fe–Mo nanoparticles. Consequently, the dominant CNT structure shifts from single- and double-walled to multi-walled, while the mean CNT diameter increases from 6.2 nm to 15.7 nm.

Compared to Fe-based catalyst, Mo/MgO exhibited a significantly lower carbon yield, with graphene identified as the dominant carbon product. This contrast highlights the critical role of Fe as the primary active element governing CNT nucleation and growth, while Mo serves as a promoter, modulating catalytic behavior without directly driving CNT formation. To further elucidate the promotional effects of Mo, the catalytic longevity of Fe/MgO, Fe–0.1Mo, and Fe–1Mo systems was systematically evaluated (Fig. S8). Both Fe/MgO and Fe–0.1Mo exhibited rapid deactivation, with carbon productivities plateauing within 30 minutes. In stark contrast, Fe–1Mo demonstrated sustained activity, with carbon productivity increasing from 15 to 60 minutes. These results underscore that optimal Mo incorporation not only enhances carbon yield but also significantly extends catalyst durability, likely by promoting Fe particle coarsening, which in turn stabilizes the active sites.

4. Conclusions

CNTs were successfully synthesized on Fe-based catalysts. Fe/MgO has a carbon productivity of 0.16 g $g_{Cat.}^{-1}$ and graphitic carbon counts for *ca.* 15% which should be mainly CNTs with 3–10 nm diameter. The incorporation of Mo not only improved the carbon production, from 0.40 g $g_{Cat.}^{-1}$ of Fe–0.1Mo to 1.03 g $g_{Cat.}^{-1}$ of Fe–1Mo, but also promoted the selectivity of graphitic carbon. In Fe–0.5Mo and Fe–1Mo catalysts, graphitic carbon selectivity exceeded 95%. With increasing Mo loading, Fe–Mo nanoparticles underwent coarsening, resulting in an increase of the average CNT inner diameter from 7.9 nm (Fe–0.1Mo) to 15.7 nm (Fe–1Mo). This catalyst particle growth mediated a transition in CNT morphology: from predominantly SWCNTs in Fe–0.1Mo to MWCNTs in Fe–0.5Mo and Fe–1Mo. Furthermore, lifetime experiments confirmed that Mo addition extended catalytic stability, with Fe–1Mo remaining active beyond 1 hour of operation. In contrast, Mo/MgO, produced graphite flakes with a low carbon productivity, underscoring the primary role of Fe in CNT growth. By adjusting the Mo loading, it is feasible to selectively synthesize SWCNTs and MWCNTs. This study provides mechanistic insights into the selective production of different types of CNTs.

Author contributions

ZP: conceptualization (lead), investigation, formal analysis, writing – original draft. FK: TEM data acquisition. PZ: nitrogen sorption data acquisition and interpretation, discussion. JAvB: conceptualization (support), funding, writing – review & editing, supervision.

Open Access Article. Published on 12 August 2025. Downloaded on 5/25/2026 12:26:41 AM. This article is licensed under a Creative Commons Attribution-NonCommercial 3.0 Unported Licence.

Conflicts of interest

There are no conflicts to declare.

Data availability

The data supporting this article have been included as part of the SI. The Supplementary Information contains additional experimental proofs, and raw data (such as more CNT images). See DOI: https://doi.org/10.1039/d5cp04231j.

Acknowledgements

The measurements were performed at the Laboratory for Catalysis and Sustainable Chemistry (LSK) of the Paul Scherrer Institute in Switzerland. This work was funded by the ETH Board in the framework of the Joint Initiative SCENE. The authors thank Dr Sandro Stucki, Dr Chiara Pischetola and Dr Sung Sik Lee for their technique assistance on TGA, XRD and Raman spectroscopy, respectively. Z. P. thanks ETH ScopeM for their support. Z. P. thanks Marcia Schoenberg for proofreading. Z. P. thanks Dr Yong Ding for her encouragement and support.

Notes and references

1 Y. H. Chan, Z. P. Chan, S. S. M. Lock, C. L. Yiin, S. Y. Foong, M. K. Wong, M. A. Ishak, V. C. Quek, S. Ge and S. S. Lam, *Chin. Chem. Lett.*, 2024, **35**, 109329.
2 G. Chen, X. Yu, K. (Ken) Ostrikov, B. Liu, J. Harding, G. Homm, H. Guo, S. A. Schunk, Y. Zhou, X. Tu and A. Weidenkaff, *Chem. Eng. J.*, 2023, **476**, 146335.
3 N. Sánchez-Bastardo, R. Schlögl and H. Ruland, *Ind. Eng. Chem. Res.*, 2021, **60**, 11855–11881.
4 T. I. Korányi, M. Németh, A. Beck and A. Horváth, *Energies*, 2022, **15**, 6342.
5 S. R. Patlolla, K. Katsu, A. Sharafian, K. Wei, O. E. Herrera and W. Mérida, *Renewable Sustainable Energy Rev.*, 2023, **181**, 113323.
6 J. Prabowo, L. Lai, B. Chivers, D. Burke, A. H. Dinh, L. Ye, Y. Wang, Y. Wang, L. Wei and Y. Chen, *Carbon*, 2024, **216**, 118507.
7 Z. Dong, B. Li, C. Cui, W. Qian, Y. Jin and F. Wei, *React. Chem. Eng.*, 2020, **5**, 991–1004.
8 A. E. Awadallah, M. A. Deyab and H. A. Ahmed, *J. Environ. Chem. Eng.*, 2021, **9**, 106023.
9 E. Lamouroux, P. Serp and P. Kalck, *Catal. Rev.*, 2007, **49**, 341–405.
10 E. Sun, S. Zhai, D. Kim, M. Gigantino, V. Haribal, O. S. Dewey, S. M. Williams, G. Wan, A. Nelson, S. Marin-Quiros, J. Martis, C. Zhou, J. Oh, R. Randall, M. Kessler, D. Kong, J. Rojas, A. Tong, X. Xu, C. Huff, M. Pasquali, R. Gupta, M. Cargnello and A. Majumdar, *Cell Rep. Phys. Sci.*, 2023, **4**, 101338.
11 M. Kim, D. Goerzen, P. V. Jena, E. Zeng, M. Pasquali, R. A. Meidl and D. A. Heller, *Nat. Rev. Mater.*, 2023, **9**, 374.
12 D. Yadav, F. Amini and A. Ehrmann, *Eur. Polym. J.*, 2020, **138**, 109963.
13 F. Ghaemi, M. Ali, R. Yunus and R. N. Othman, *Synthesis, Technology and Applications of Carbon Nanomaterials*, Elsevier, 2019, pp. 1–27.
14 M. V. Kharlamova, *Beilstein J. Nanotechnol.*, 2017, **8**, 826–856.
15 W. Lu, T. He, B. Xu, X. He, H. Adidharma, M. Radosz, K. Gasem and M. Fan, *J. Mater. Chem. A*, 2017, **5**, 13863–13881.
16 D. Wang, J. Zhang, J. Sun, W. Gao and Y. Cui, *Int. J. Hydrogen Energy*, 2019, **44**, 7205–7215.
17 D. Torres, J. L. Pinilla, M. J. Lázaro, R. Moliner and I. Suelves, *Int. J. Hydrogen Energy*, 2014, **39**, 3698–3709.
18 W.-M. Yeoh, K.-Y. Lee, S.-P. Chai, K.-T. Lee and A. R. Mohamed, *J. Alloys Compd.*, 2010, **493**, 539–543.
19 S. Tang, Z. Zhong, Z. Xiong, L. Sun, L. Liu, J. Lin, Z. X. Shen and K. L. Tan, *Chem. Phys. Lett.*, 2001, **350**, 19–26.
20 W. E. Alvarez, B. Kitiyanan, A. Borgna and D. E. Resasco, *Carbon*, 2001, **39**, 547–558.
21 Z. Li, J. A. Larsson, P. Larsson, R. Ahuja, J. M. Tobin, J. O'Byrne, M. A. Morris, G. Attard and J. D. Holmes, *J. Phys. Chem. C*, 2008, **112**, 12201–12206.
22 Q. Li, Y. Hao, C. Yan, Z. Jin and L. Zhongfan, *J. Mater. Chem.*, 2002, **12**, 1179–1183.
23 G. Ning, Y. Liu, F. Wei, Q. Wen and G. Luo, *J. Phys. Chem. C*, 2007, **111**, 1969–1975.
24 J. C. Yu, A. Xu, L. Zhang, R. Song and L. Wu, *J. Phys. Chem. B*, 2004, **108**, 64–70.
25 M. A. Azab, A. E. Awadallah, A. A. Aboul-Enein and S. A. Hassan, *Fullerenes, Nanotubes Carbon Nanostruct.*, 2023, **31**, 109–119.
26 N. R. E. Radwan, A. M. Ghozza and G. A. El-Shobaky, *Thermochim. Acta*, 2003, **398**, 211–221.
27 R. Salomão and V. C. Pandolfelli, *Ceram. Int.*, 2008, **34**, 1829–1834.
28 E. Lamouroux, P. Serp, Y. Kihn and P. Kalck, *Appl. Catal., A*, 2007, **323**, 162–173.
29 S. B. X. Y. Zhang, Q. Pessemesse, L. Lätsch, K. M. Engel, W. J. Stark, A. P. Van Bavel, A. D. Horton, P.-A. Payard and C. Copéret, *Chem. Sci.*, 2023, **14**, 5899–5905.

 This journal is © the Owner Societies 2025